

# Eccentricity design for the coolant distribution optimization of a practical commercial-size proton exchange membrane fuel cell stack using a novel proper orthogonal decomposition based analysis model

Fan Bai<sup>a</sup>, Ren-Jie Yin<sup>a</sup>, Jin-Yang Liao<sup>b,c</sup>, Zhuo Zhang<sup>a</sup>, Sai-Jie Cai<sup>a</sup>, Yu-Tong Mu<sup>d</sup>, Li Chen<sup>a</sup>, Lei Chen<sup>a</sup>, Wen-Quan Tao<sup>a,\*</sup>

<sup>a</sup> Key Laboratory of Thermo-Fluid Science & Engineering of MOE, Xi'an Jiaotong University, Xi'an, Shaanxi 710049, PR China

<sup>b</sup> Dongfang Electric (Chengdu) Hydrogen Fuel Cell Technology Co., Ltd., Chengdu, Sichuan 611731, PR China

<sup>c</sup> Long Life Fuel Cell Key Laboratory of Sichuan Province, Chengdu, Sichuan 611731, PR China

<sup>d</sup> School of Human Settlements and Civil Engineering, Xi'an Jiaotong University, Xi'an, Shaanxi 710049, PR China

## HIGHLIGHTS

- Carefully tested grid-independence for the refined simulation requirement.
- Proposed a POD based method for flow distribution analysis.
- Explicit expression between coolant distribution curve and eccentricity.
- Finding the optimal eccentricity of 0.8856.
- 4.04-times reduction of the coolant distribution non-uniformity.

## ARTICLE INFO

### Keywords:

Proton exchange membrane fuel cell stack  
Thermal management  
Coolant distribution optimization  
Explicit mathematical expression  
Proper orthogonal decomposition

## ABSTRACT

The uniform distribution of coolant among different coolant flow field plates is of critical importance to the thermal management of proton exchange membrane fuel cell (PEMFC) stacks. Herein, the coolant distribution uniformity is optimized using an eccentric end socket structure based on the computational fluid dynamic (CFD) method. Firstly, the grid systems are comprehensively tested for the refined simulation requirements under a well-distributed condition and a high current density. Then, to reduce the heavy burden of computing resources, a novel analysis model is proposed to further establish the explicit mathematical expression between the coolant distribution curve (CDC) and the eccentricity based on the CFD results and proper orthogonal decomposition (POD). Finally, the coolant distribution uniformity is optimized according to the above explicit expression. Results suggest that for the studied cases, the grid systems with the manifold cross section grid numbers take 4 480 and 8 385 can be regarded as the grid-independent ones under the eccentricity ranges of 0 ~ 0.7 and 0.7 ~ 1.0 respectively. The simulated stack pressure drops show a high consistence with the experimental ones with a maximum relative deviation of 10%, validating the reliability of the CFD model. With the increase of the eccentricity, the coolant distribution non-uniformity decreases firstly and finally increase. The CDCs are similar if the eccentricity vector points to the same side of the transverse eccentricity axis. The optimized coolant distribution non-uniformity (1.58%) reduces 4.04 times compared with that in the benchmark case (6.38%) when the eccentricity takes 0.8856.

## 1. Introduction

Renewable-powered green hydrogen production is crucial for

carbon-neutral industry [1,2]. To date, proton exchange membrane fuel cell (PEMFC) is one of the most important power generating facilities utilizing hydrogen [3]. With the accelerating application scopes [4] of PEMFCs around the world, for instance, transportation, stationary,

\* Corresponding author.

E-mail address: [wqtao@mail.xjtu.edu.cn](mailto:wqtao@mail.xjtu.edu.cn) (W.-Q. Tao).

<https://doi.org/10.1016/j.apenergy.2023.121389>

Received 6 March 2023; Received in revised form 2 May 2023; Accepted 31 May 2023

Available online 17 June 2023

0306-2619/© 2023 Published by Elsevier Ltd.

Nomenclature			
<i>Symbol</i>		$r_l$	Longitudinal component of the axis distance vector, [m]
$A$	Half of the manifold cross section length, [m]	$r_t$	Transverse component of the axis distance vector, [m]
$\mathbf{a}$	Coolant distribution curve on the mode space	$S_{u,j}$	Momentum source term, [N·m <sup>-3</sup> ]
$B$	Half of the manifold cross section width, [m]	$\mathbf{U}$	Left singular vectors
$C_{IR}$	Inertial resistance coefficient, [m <sup>-1</sup> ]	$u_i$	Superficial velocity in porous media, [m·s <sup>-1</sup> ]
$C_{VR}$	Viscous resistance coefficient, [m <sup>-2</sup> ]	$\mathbf{V}$	Right singular vectors
$C_{\mu}, C_{1\epsilon}, C_{2\epsilon}$	Constants	$x_i$	Direction vector, [m]
$\mathbf{E}$	Eccentricity vector	$\gamma$	Porosity
$E$	Eccentricity	$\Delta$	Non-uniformity
$E_l$	Longitudinal eccentricity	$\delta_{ij}$	Kronecker symbol
$E_t$	Transverse eccentricity	$\epsilon$	Turbulence fluctuation kinetic energy dissipation rate, [m <sup>2</sup> ·s <sup>-3</sup> ]
$e_c$	The major flow direction in the single coolant flow field plates	$\chi_i$	Coolant distribution curve
$e_l$	Positive direction of the longitudinal eccentricity	$\chi'_i$	Influence of vortex on coolant distribution curve
$e_t$	Positive direction of the transverse eccentricity	$\theta$	Argument
$\mathcal{F}$	Space transformation	$\mu$	Molecular viscosity, [Pa·s]
$G_k$	Turbulence kinetic energy generation due to local mean velocity gradient, [kg·m <sup>-1</sup> ·s <sup>-3</sup> ]	$\mu_e$	Effective viscosity, [Pa·s]
$g$	Gravitational acceleration, [m·s <sup>-2</sup> ]	$\mu_r$	Relative viscosity in the porous medium
$k$	Turbulence fluctuation kinetic energy, [m <sup>2</sup> ·s <sup>-2</sup> ]	$\mu_t$	Turbulent viscosity, [Pa·s]
$l$	Truncation order	$\rho$	Density, [kg·m <sup>-3</sup> ]
$N$	Number of coolant flow field plates	$\Sigma$	Singular value matrix
$n$	Mode number	$\sigma$	Singular value
$Pr$	Prandtl number	$\psi$	Mode
$p$	Pressure, [Pa]	<i>Abbreviation</i>	
$q_{m,0}$	Average mass flow rate through each coolant flow field plate	CDC	Coolant distribution curve
$q_{m,i}$	Mass flow rate through each coolant flow field plate	CFD	Computational fluid dynamic
$R^2$	R-squared	CFP	Coolant flow field plate
$Re$	Reynolds number	FNM	Flow network model
$\mathbf{r}$	Axis distance vector, [m]	PEMFC	Proton exchange membrane fuel cell
		POD	Proper orthogonal decomposition
		s.t.	Subject to
		UDF	User defined function

auxiliary and portable devices, etc. [5], the performance investigation of PEMFC stacks is of critical significance to the ever-accelerating commercial-size application.

Thermal management is one of the most critical issues in PEMFC stack investigation [6]. On the one hand, a high operational temperature will result in membrane dehydration, leading to reductions of performance and device durability. On the other hand, a low operational temperature will result in the flooding of electrodes, leading to an additional resistance in reactant mass transfer process. Therefore, an appropriate operational temperature range, generally within 60–80 °C [7], exists for a given PEMFC stack. In the high-power applications scenarios of PEMFCs, plenty of waste heat, even comparable to the output electrical power [6,8,9], dissipates due to the electrochemical reaction and the transport processes. To avoid the deterioration of thermal management, the waste heat must be timely taken away. Single-phase forced convection liquid cooling is the most widespread cooling strategy in the scenarios due to appropriate heat transfer coefficients [9,10]. The coolant firstly flows into an inlet manifold through an inlet end socket, and then distributes into each single coolant flow field plate (CFP) from the manifold, finally flows out of the stack through an outlet manifold and an outlet end socket. Insufficient coolant flow rates for several CFPs will lead to higher temperatures in the corresponding single cells. Therefore, coolant distribution uniformity is one of the most important factors affecting the thermal management of PEMFC stacks [5,11].

During the past two decades, the PEMFC stack flow distribution uniformity, defined by the flow rate (through each flow field plate) uniformity of the reactants or coolant in the studied PEMFC stack, has been widely studied. In the following, unless the 'coolant' is

emphasized, the presenting flow distribution researches represent that in the anode, cathode or coolant due to the extremely similar research methodology. Due to the difficulty to deposit sensors testing the flow rate in each single cell, there are very limited researches investigating the flow distribution uniformity in PEMFC stacks by an experimental approach [12]. Modeling, represented by a computational fluid dynamic (CFD) model and a flow network model (FNM), is the most famous research procedure. CFD models are the most comprehensive prediction model which can also be regarded as the standard solution inspecting the reliability of FNMs [13]. In CFD models, the velocity and pressure fields in the studied PEMFC stack are simulated numerically. And then the flow distribution of each single cell can be obtained by the statistical results from the simulated fields. In contrary, in FNMs, the fluid flow in PEMFC stacks is modelled by an analogy with circuits. And then the flow distribution can be obtained by the solution of simultaneous equations. Till now, FNMs [13–20] have been more widely adopted by researchers benefiting from the prediction efficiency. However, the possible vortices generated in the manifold are very difficult to be modelled in FNMs. In view of this, a CFD model is adopted in this paper.

After a survey of 12 journal articles on CFD models [4,12,13,21–29], a few important observations are summarized below.

- Two literatures report 2D simulation and 10 literatures report 3D simulation. 3D simulation can predict the flow field in the manifold more precisely, therefore is more widely adopted in the literatures.
- In the researches with the cell number larger than 100, 93 flow distribution curves are presented. The reported current density and flow distribution non-uniformity (defined as the difference

between the maximum and minimum single cell mass flow rates divided by the average one) frequency distribution diagrams are shown in Fig. 1. From Fig. 1 (b), it can be seen that most of the reported flow distribution non-uniformities are up to several tens of percent and even exceed 100%. As far as the grid number is concerned, the maximum grid number is  $1.2 \times 10^7$  and millions of grid cells are adopted in a majority of the researches. However, these results may not sufficiently guide the flow distribution design for the practical commercial-size PEMFC stack. In the practical commercial-size PEMFC stack, a flow distribution non-uniformity less than 10% is highly required. During the manifold design under this flow distribution non-uniformity level, due to a tiny mass flow rate difference between the adjacent cells, a highly refined simulation is required, but the numerical uncertainty caused from the computational domain discretization has not been carefully analyzed especially for the manifold with complex end socket. It can also be found that only 12.9% of the flow distribution curves (only in one paper [28]) are reported within the high current density range ( $\geq 1.8 \text{ A}\cdot\text{cm}^{-2}$ ), which is also an important condition during practical PEMFC stack operation. Besides, with the increase of the load (current density), the total coolant flow rate will also increase, and thus the flow distribution uniformity among cells or CFPs will deteriorate rapidly especially in the high current density range. Therefore, it is of crucial necessity and urgency for the coolant flow distribution analyses and optimizations for the practical commercial-size PEMFC stack especially under the highest working current density.

- (c) Most of the researchers present, compare and analyze the flow distribution curve only under several groups of conditions. Chen et al. [26] goes further and establishes machine learning models to characterize the correlation between the pressure uniformity and several design parameters. However, the models can only predict pressure uniformity, and fail to predict the whole flow distribution curve. Furthermore, the method can only obtain an implicit machine learning model instead of an explicit mathematical expression.
- (d) Only a few literatures focus on the design of vortexes for the flow distribution optimization. Previous researchers introduce the vortexes in the manifold to improve the flow distribution uniformity using an eccentric end socket by designing the feed header's configuration [28], tube-to-intermediate zone length ratio [26,28], intermediate zone width [26], and the ratio of inlet tube to manifold hydraulic diameter [26,28]. The above studies make important contribution for the flow distribution uniformity improvements. However, it is the eccentric structure in the inlet

end socket that directly drives the vortexes in the manifold. The impact of the eccentricity on the flow distribution curve has not been adequately studied. Therefore, the eccentricity is selected as a design parameter in this paper.

This paper pertains to optimize the coolant distribution uniformity for a practical commercial-size PEMFC stack by designing the end socket based on a 3D porous medium CFD approach under a high current density. The grid systems are comprehensively tested for the refined simulation requirements. A novel data analysis model is proposed to establish the explicit mathematical expression between coolant distribution curve (CDC) and design parameters based on proper orthogonal decomposition (POD), to reduce the heavy burden of computing resources in the manifold and end socket design. In the remainder of this paper, the modeling methodology is introduced in Section 2. Then, the results are exhibited and discussed in Section 3. Finally, conclusions are drawn in Section 4.

## 2. Methodology

The methodology of implementing efficient simulation proposed in this paper consists of two main submodules: (1) a CFD model, which is used to determine coolant distribution curve under one given group of conditions; (2) a POD based analysis model, which establishes the explicit mathematical expression between CDC and design parameters within the entire studied range. In the following of this section, the two submodules will be described in Subsections 2.1 and 2.2 sequentially. The experimental setup will be presented in Subsection 2.3.

### 2.1. Computational fluid dynamic model

#### 2.1.1. Computational domain and grid system

In this research, the coolant flow field with U-type configuration in a commercial-size PEMFC stack with  $320 \text{ cm}^2$  activation area and 141 CFPs is studied. The computational domain and grid system are shown in Fig. 2. The computational domain consists of the end sockets, the manifolds and the CFPs simulated by porous medium. The manifold and the CFPs are remained the same in this research, and only the socket part is studied. The inlet and outlet end sockets are identical in each studied case. Due to the coolant is separated with the reactants, the multi-physics fields in the anode and cathode are not simulated. As shown in Fig. 2, patched three-block grid system is generated for simulation. The 2D 'ogrid block' grid and the entire 3D grid are generated using ANSYS ICEM 2019 R2 and Altair Hypermesh 2019 respectively.

As shown in Fig. 3, the eccentricity vector ( $\mathbf{E}$ ) is defined as the axis distance vector (from the axis of the manifold to the axis of the inlet

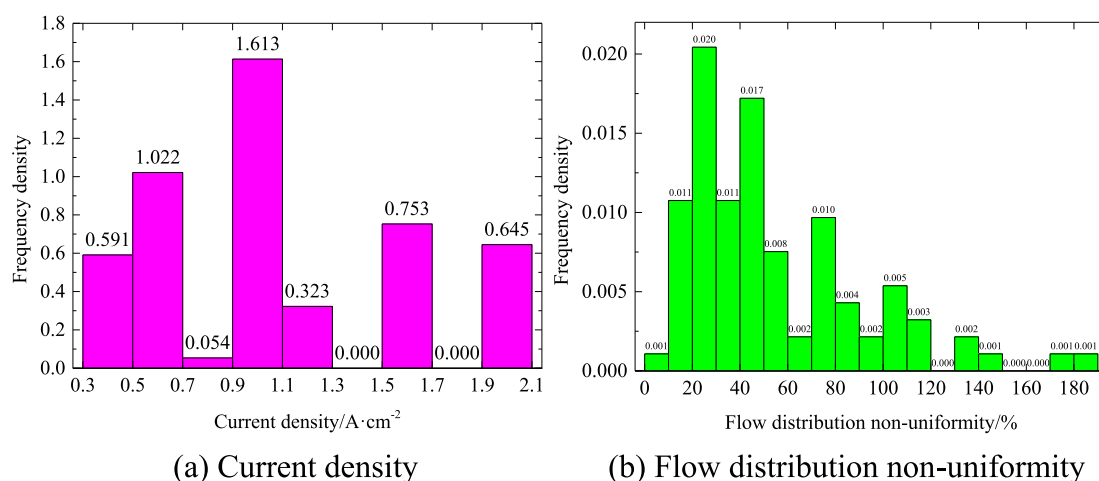


Fig. 1. Current density and flow distribution non-uniformity frequency distribution histograms reported in the literatures.

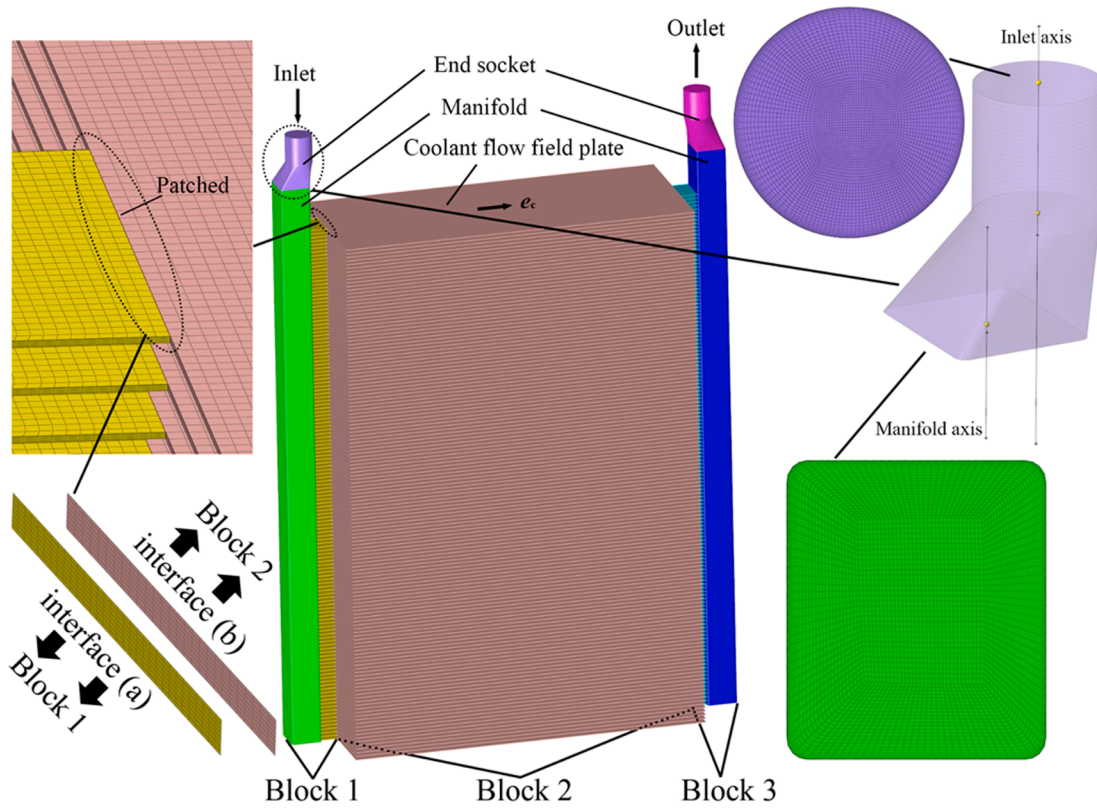


Fig. 2. Computational domain and grid system.

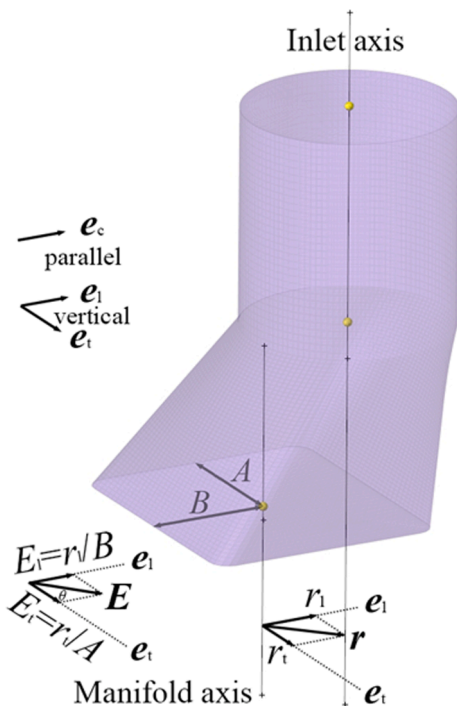


Fig. 3. Sketch map of the eccentricity vector ( $E$ ) definition.

surface) normalized by the characteristic length in the transverse and longitudinal directions, defined as the perpendicular and parallel directions to the major flow direction in CFPs respectively. The characteristic length of each direction is selected as half of the manifold magnitude in the direction.  $E$  can be decomposed into two components,

transverse eccentricity ( $E_t$ ) and longitudinal eccentricity ( $E_l$ ). The positive directions of the eccentricities are pointing in the inner direction between the axes of inlet and outlet manifolds. For example, in the studied PEMFC stack shown in Fig. 2, the major flow direction in CFPs, the positive directions of the transverse and longitudinal eccentricities are marked as  $e_c$ ,  $e_t$  and  $e_l$  respectively in Fig. 3. The axis distance vector is marked as  $r$ . The two components of the eccentricity vector can be calculated as  $(r_t/A, r_l/B)$ . The magnitude and argument of the above eccentricity vector is marked as  $E$  (eccentricity) and  $\theta$  (argument) respectively. In this paper, they are selected as the two variable geometrical parameters for vortex design in the manifold. The condition of each simulated case is shown in Table 1. Cases 0 ~ 4 are designed for investigating the impact of eccentricity on CDC. Cases 1, 5 ~ 11 are designed for investigating the impact of argument on CDC.

### 2.1.2. Assumptions

- (1) Coolant flow is incompressible and in steady state.
- (2) The back pressure is defined as the reference pressure. Therefore, the relative pressure in the outlet surface is set as 0.
- (3) The flow in the manifold ( $Re_{in} \approx 1.26 \times 10^5$ ) is turbulent while that in the CFP ( $Re \approx 1200$ ) is laminar.
- (4) The PEMFC stack is well sealed and the leakage among the anode, cathode, coolant and the stack outside are neglected.
- (5) The influence of temperature non-uniformity on the coolant physical properties is neglected because the temperature difference between the coolant inlet and outlet is small (within  $8^\circ\text{C}$ ). The average temperature is selected as the reference temperature to determine the physical properties.
- (6) The CFP region is simplified as an integrated porous medium.
- (7) The enhanced wall function treatment [30] is adopted for the accurate simulation of the flow boundary layer.

**Table 1**  
Variable design geometrical parameters of each simulated case.

No.	0	1	2	3	4	5	6	7	8	9	10	11
$E$	0	0.35	0.7	0.85	1.0	0.35	0.35	0.35	0.35	0.35	0.35	0.35
$\theta$	0	0	0	0	0	45°	90°	135°	180°	225°	270°	315°

**2.1.3. Governing equations**

The coolant flow is governed by the continuity equation and the momentum equation, as shown in Eqs. (1) and (2).

$$\frac{\partial}{\partial x_i}(\rho u_i) = 0 \tag{1}$$

$$\frac{\partial}{\partial x_i} \left( \frac{\rho u_i u_j}{\gamma^2} \right) = -\frac{\partial p}{\partial x_j} + \frac{\partial}{\partial x_i} \left( \mu_e \frac{\partial}{\partial x_i} \left( \frac{u_j}{\gamma} \right) \right) + \frac{\partial}{\partial x_i} \left( \mu_e \frac{\partial}{\partial x_j} \left( \frac{u_i}{\gamma} \right) \right) - \frac{2}{3} \frac{\partial}{\partial x_j} \left( \mu_e \frac{\partial}{\partial x_i} \left( \frac{u_i}{\gamma} \right) \right) + S_{u_j} \tag{2}$$

where  $x_i$  is the direction vector component,  $\rho$  is the coolant density,  $u_i$  is the superficial velocity in porous media,  $\gamma$  is the porosity (takes 1 in manifolds and end sockets),  $p$  is the relative pressure,  $\mu_e$  is the effective viscosity and  $S_{u_j}$  is the momentum source term which can be calculated by Eq. (3).

$$S_{u_j} = \delta_{j1} \rho_g g - \left( C_{VR} \mu u_j + C_{IR} \frac{1}{2} \rho \sqrt{(u_i u_i)} u_j \right) \tag{3}$$

where  $g$  is the gravitational acceleration.  $\delta_{j1}$  is the Kronecker symbol meaning that the direction of the gravitational acceleration towards the positive direction of the 1st axis ( $x$  axis).  $C_{VR}$  and  $C_{IR}$  are the viscous and inertial resistance coefficients respectively (take 0 in manifolds and end sockets).  $\mu_e$  can be calculated by Eq. (4) [31,32].

$$\mu_e = \mu \mu_r + \mu_t \tag{4}$$

where  $\mu$ ,  $\mu_r$  and  $\mu_t$  (takes 0 in laminar regions) are the molecular viscosity, relative viscosity in the porous medium and the turbulent viscosity respectively.

In turbulent regions,  $\mu_t$  can be calculated as Eq. (5).

$$\mu_t = \rho C_\mu \frac{k^2}{\varepsilon} \tag{5}$$

where  $C_\mu$  is a constant.  $k$  and  $\varepsilon$  are the turbulence fluctuation kinetic energy and its dissipation rate respectively. For calculating the turbulent viscosity in Eq. (5), the standard  $k-\varepsilon$  model is adopted. The governing equations are shown in Eqs. (6) and (7).

$$\frac{\partial}{\partial x_i}(\rho u_i k) = \frac{\partial}{\partial x_j} \left[ \left( \mu + \frac{\mu_t}{Pr_k} \right) \frac{\partial k}{\partial x_j} \right] + G_k - \rho \varepsilon \tag{6}$$

$$\frac{\partial}{\partial x_i}(\rho u_i \varepsilon) = \frac{\partial}{\partial x_j} \left[ \left( \mu + \frac{\mu_t}{Pr_\varepsilon} \right) \frac{\partial \varepsilon}{\partial x_j} \right] + C_{1\varepsilon} \frac{\varepsilon}{k} G_k - C_{2\varepsilon} \rho \frac{\varepsilon^2}{k} \tag{7}$$

where  $Pr_k$ ,  $Pr_\varepsilon$ ,  $C_{1\varepsilon}$ ,  $C_{2\varepsilon}$  are constants.  $G_k$  is the turbulence kinetic energy generation due to local mean velocity gradient, which can be calculated by Eq. (8).

$$G_k = \mu_t \frac{\partial u_i}{\partial x_j} \left( \frac{\partial u_i}{\partial x_j} + \frac{\partial u_j}{\partial x_i} \right) \tag{8}$$

All the modeling parameters in Eqs. (1)–(8) are summarized in Table 2. The three porous parameters,  $\gamma$ ,  $C_{VR}$  and  $C_{IR}$ , will be discussed in Subsection 3.1.

It should be noted that in Table 2, the relative viscosity takes 1 instead of other correlations (as functions of porosity) for porous media as adopted in literatures [33,34]. This is because it is the pressure difference across the CFP that drives the flow through it. The correlation

**Table 2**  
Parameters in the computational fluid dynamic model.

No.	Parameter	Value
1	$\rho$	998 kg·m <sup>-3</sup> (20 °C) 978 kg·m <sup>-3</sup> (69 °C)
2	$\mu$	1.003 × 10 <sup>-3</sup> kg·m <sup>-1</sup> ·s <sup>-1</sup> (20 °C) 4.092 × 10 <sup>-4</sup> kg·m <sup>-1</sup> ·s <sup>-1</sup> (69 °C)
3	$\mu_r$	1
4	$g$	9.8 m·s <sup>-2</sup>
5	$C_\mu$	0.09
6	$C_{1\varepsilon}$	1.44
7	$C_{2\varepsilon}$	1.92
8	$Pr_k$	1
9	$Pr_\varepsilon$	1.3

between the pressure difference and mass flow rate for the studied CFP is the most important parameter influencing the CDC. Therefore, as long as  $C_{VR}$  and  $C_{IR}$  take proper values to guarantee a correct correlation between the CFP pressure difference and the mass flow rate, the CDC will be simulated correctly. This is the reason why the relative viscosity takes 1 in this research.

**2.1.4. Numerical procedure**

The above governing equations are solved by the finite volume method (FVM) in ANSYS FLUENT 17.2. SIMPLE algorithm is adopted for the pressure–velocity coupling. Second order upwind difference is adopted for the convection term discretization in the momentum,  $k$  and  $\varepsilon$  governing equations. The data exchange between different blocks across interfaces is implemented in the FLUENT solver. The relative deviation of the mass flow rate for each CFP  $\chi_i$  ( $1 \leq i \leq N$ ,  $i$  represents the index of CFP,  $i = 1$  represents the nearest CFP from the stack inlet) is defined as the relative deviation of the mass flow rate through each CFP ( $q_{m,i}$ ) to the average one ( $q_{m,0}$ ), as shown in Eq. (9).

$$\chi_i = \frac{q_{m,i} - q_{m,0}}{q_{m,0}} \times 100\% \tag{9}$$

If the coolant distribution is extremely even,  $\chi_i$  takes 0 for each CFP. In each case,  $\chi_i$  can be obtained from the statistical result of the velocity field using self-developed user defined function (UDF). The variation curve between  $\chi_i$  and CFP index  $i$  under one condition forms a CDC. Then the non-uniformity ( $\Delta$ ) can be defined by Eq. (10).

$$\Delta = \max(\chi_i) - \min(\chi_i) \tag{10}$$

It should be emphasized that in this paper, the range of  $\chi_i$  ( $\Delta$ ) is selected as the definition of the flow distribution non-uniformity criterion instead of the more widely adopted criterion in several previous literatures, the standard deviation [4,13,28]. This is because it is the extremum of the thermal management that will lead to the flooding or the membrane dehydration. The range of  $\chi_i$  ( $\Delta$ ) can exhibit the above extremum information better compared with the standard deviation, therefore is adopted in this paper. Furthermore, the conventional convergence criteria (i.e., residuals < 10<sup>-4</sup>) are not sufficient for this simulation due to the refined simulation requirement for capturing the tiny mass flow rate difference between the adjacent CFPs. The convergence criterion of the simulations in this paper is that the maximum absolute change of each point on the CDC is lower than 0.01% within at least 2 000 iterations. A typical convergent simulation requires 20 000 ~ 200 000 iterations. The most time-consuming simulation (grid number: 298 million) in this paper takes 6.17 days even by 1008-core

parallel simulation. Furthermore, the R-squared value [35] is adopted to judge if one curve  $\chi_{i,1}$  is identical with the standard one  $\chi_{i,0}$ , as shown in Eq. (11).

$$R^2 = 1 - \frac{\sum_{i=1}^N (\chi_{i,1} - \chi_{i,0})^2}{\sum_{i=1}^N (\chi_{i,0} - \frac{1}{N} \sum_{j=1}^N \chi_{j,0})^2} \quad (11)$$

In this research, two curves are regarded as identical if R-squared is higher than 0.98.

## 2.2. POD based analysis model

The computational fluid dynamic model described in Subsection 2.1 is time-consuming. It is extremely uneconomical to simulate CDCs under lots of conditions for design. A more feasible and economical strategy is to simulate CDCs under a small number of conditions by the CFD approach firstly. And then establish a correlation between CDC and design parameters within the studied ranges. Finally, the coolant distribution uniformity can be optimized based on the above correlation. However, the dependent variable of the above correlation is the whole curve, leading to the modeling difficulty. A POD based analysis model is proposed to establish the above correlation. The centerpiece of this model is to analyze CDC in a low-order mode space, similar to the spectrum map analysis in the Fourier series. In this subsection, the algorithm of the analysis model will be introduced. Details about the principle of POD can be referred to [36].

The sketch map of the model is shown in Fig. 4. An example of the original CDC is shown in Fig. 4 (a). The influence of vortex on CDC ( $\chi'_i$ ) is defined as the additional curve after introducing the eccentric end socket structure, as shown in Eq. (12).

$$\chi'_i = \chi_i - \chi_{i,0} = \chi_i - a_0 \psi_{i,0} \quad (12)$$

where  $\chi_{i,0}$  is the CDC using the non-eccentric end socket structure (Case 0 in Table 1).  $a_0$  and  $\psi_{i,0}$  are the magnitude and normalization mode of  $\chi_{i,0}$ .  $\chi_i$  can be expressed as the formation of modal superposition, as

shown in Fig. 4 (b) and Eq. (13).

$$\chi_i = \sum_{j=0}^n a_j \psi_{i,j} \quad (13)$$

where each  $\psi_j$  (columns of  $\psi_{i,j}$ ,  $1 \leq j \leq n$ ) is the normalization mode capturing each characteristic of  $\chi'_i$ ,  $n$  is the mode number,  $a_j$  is the projection of  $\chi'_i$  on the corresponding mode. Finally, the original CDC  $\chi_i$  is transformed into the mode space expression  $a_j$ , as shown in Fig. 4 (c) and Eq. (14).

$$a = \mathcal{F}(\chi) \quad (14)$$

where  $\mathcal{F}$  represents the space transformation.

From the above discussion, it can be seen that the basic problem of the analysis consists of two parts. (a) How to construct the mode space? (b) How to establish the correlation between CDC and design parameters in the mode space?

### 2.2.1. How to construct the mode space?

POD is a feasible approach to construct the above mode space for order reduction. The snapshot matrix  $\chi'_{i,m}$  is formed by combining all the vectors  $\chi'_i$  obtained from the pre-simulated CDCs. The singular value decomposition of  $\chi'_{i,m}$  is expressed as Eq. (15).

$$\mathbf{X}' = \mathbf{U}\mathbf{\Sigma}\mathbf{V}^* \quad (15)$$

where  $\mathbf{U}$  and  $\mathbf{V}$  are unitary matrices called left and right singular vectors respectively.  $\mathbf{\Sigma}$  is the non-square diagonal matrix storing the singular value  $\sigma$  of each singular vector, representing the amount of information captured by the corresponding singular vector.  $*$  represents the matrix transpose. After right multiplying the snapshot matrix  $\mathbf{X}'$  by  $\mathbf{V}$  and normalization, the mode space  $\psi_{i,j}$  can be constructed, as shown in Eq. (16).

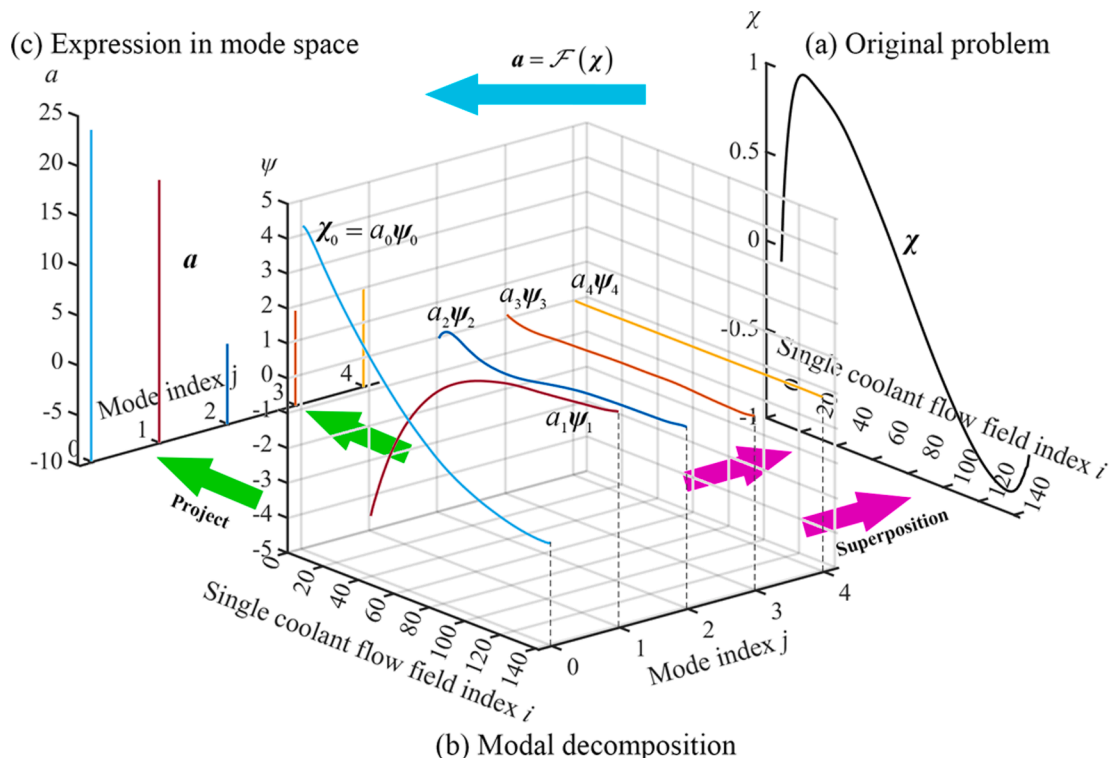


Fig. 4. Sketch map of the POD based analysis model.

$$\psi_j = \frac{\sum_{m=1}^n \chi'_m V_{m,j}}{\|\sum_{m=1}^n \chi'_m V_{m,j}\|} \quad (16)$$

where  $\|\cdot\|$  represents the L2 norm.

Due to the information concentration property of each  $\psi_j$ , after sorting  $\psi_j$  by the descending order of the respective singular value  $\sigma_j$ , the secondary dimensions can be neglected. Therefore, the order of the original problem is further reduced. The considering information is regarded as sufficient if the modes capture more than 99% of the total information. Therefore, the truncation order  $l$  is defined by Eq. (17).

$$\begin{cases} \min : & l \\ \text{s. t.} & \frac{\sum_{j=1}^l \sigma_j}{\sum_{j=1}^n \sigma_j} > 99\% \end{cases} \quad (17)$$

### 2.2.2. How to establish the correlation between CDC and design parameters in the mode space?

After the above step, CDC can be transformed into the  $l$ -dimension mode space with the coordinate axes (mode) of  $\psi_j$  and the coordinates of  $a_j$ . Once each coordinate  $a_j$  is known, CDC can be obtained by Eq. (18).

$$\chi_i = \sum_{j=0}^l a_j \psi_{i,j} \quad (18)$$

Each coordinate  $a_j$  is a function ( $f_j$ ) of design parameters, as shown in Eq. (19).

$$a_j = f_j(\mathbf{E}) \quad (19)$$

The coordinates at snapshot conditions can be projected by Eq. (20).

$$a_{j,m} = \sum_{i=1}^N \psi_{i,j} \chi'_{i,m} \quad (20)$$

Then, the function  $f_j$  in Eq. (19) is obtained by the cubic spline interpolation. The algorithms in Subsection 2.2 are realized by self-programming in MATLAB R2021a.

### 2.3. Experimental setup

The experimental system to test the PEMFC stack pressure drop for the following calibration process is shown in Fig. 5. It consists of the PEMFC stack, pressure test system and temperature test system. Four-way ferrules are installed on the coolant inlet and outlet pipelines of the stack. The temperature sensors and the pressure sensors are installed at the other two sides of the four-way ferrules respectively and parallel to the ground. The sensors are 5 ~ 7 cm away from the PEMFC stack inlet and outlet end sockets. The specification of the pressure sensor is Dwyer 626-09-GH-P1-E1-S1. The range is 0 ~ 50 PSIG. The precision is  $\pm 0.25\%$  (full scale).

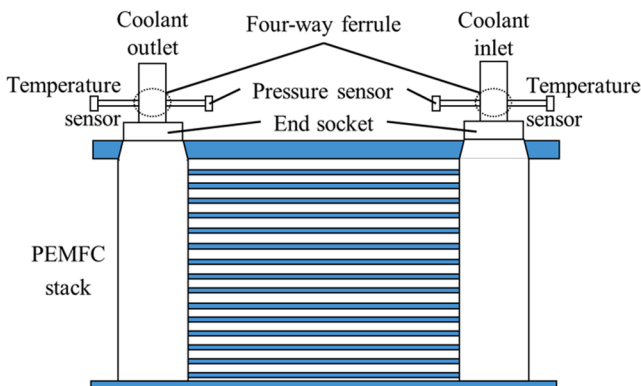


Fig. 5. Experimental setup (vertical view).

### 3. Results and discussion

The developed CFD and analysis models in Section 2 are now used to optimize coolant distribution uniformity by designing the eccentricity vector of the end socket for the PEMFC stack shown in Fig. 2. The coolant flow field is designed with a serpentine configuration. The mass flow rates of all the cases are  $0.01 \text{ kg}\cdot\text{s}^{-1}\cdot\text{CFP}^{-1}$  (current density:  $1.8 \text{ A}\cdot\text{cm}^{-2}$ ). In general, under one given condition, the higher the working current density is, the worse the coolant distribution uniformity is. Therefore, in this paper, only the coolant distribution uniformity under the highest load of the commercial application is optimized. In the following, the determination of the three porous medium parameters,  $\gamma$ ,  $C_{VR}$  and  $C_{IR}$ , will firstly be presented in Subsection 3.1. The CFD model will be comprehensively validated in Subsection 3.2. Later, the impacts of the eccentricity and argument on CDC will be presented and analyzed in Subsections 3.3 and 3.4 respectively. Finally, the optimal eccentricity vector will be designed in Subsection 3.5.

#### 3.1. Determination of the porous medium parameters

This subsection presents the determination of the three porous parameters,  $\gamma$ ,  $C_{VR}$  and  $C_{IR}$  in Eq. (3). Porosity  $\gamma$  is computed directly by dividing the volume of actual coolant flow field by the volume of porous simplified coolant flow field.  $C_{VR}$  and  $C_{IR}$  can be calibrated by a trial-and-error approach from the experimental correlation between the pressure and mass flow rate. The calibrated stack contains 15 CFPs. The experimental and simulated correlations between the 15-CFP stack pressure drop and mass flow rate are shown in Fig. 6. R-squared is 0.995, showing a high matching degree between experimental and simulated results. The temperature, eccentricity vector, porosity  $\gamma$ ,  $C_{VR}$  and  $C_{IR}$  take  $20^\circ\text{C}$ , (0.42, 0.05), 0.376,  $2.12 \times 10^8 \text{ m}^{-2}$  and  $617 \text{ m}^{-1}$  respectively.

#### 3.2. Validations of the computational fluid dynamic model

This subsection validates the CFD model presented in Subsection 2.1 for predicting the CDC of the 141-CFP PEMFC stack (stack hereafter in this paper represents 141-CFP PEMFC stack) in the aspects of comprehensive grid-independent tests, selection of turbulent model, the experimental validation. In the following they will be presented in order.

##### 3.2.1. Grid-independent test

In flow distribution phenomenon, the pressure drops through one

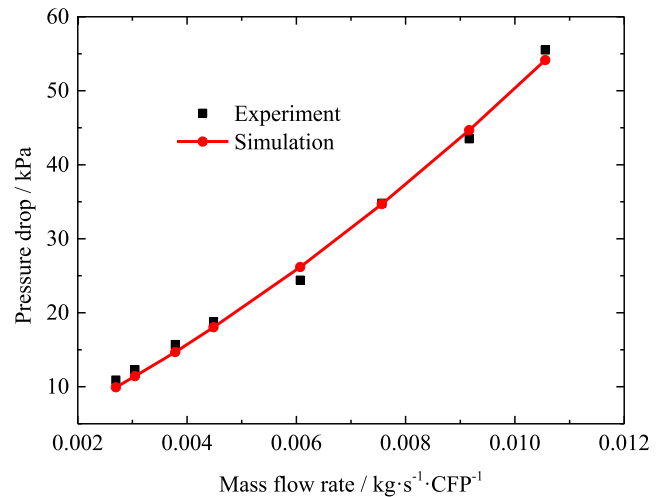


Fig. 6. Experimental and simulated correlations between 15-CFP stack pressure drop and mass flow rate.

single cell (or CFP) and the manifold are crucial factors influencing CDC. Furthermore, the CDCs under zero, medium and high eccentricities are important output characteristics. The grid-independent tests are implemented in the above aspects.

- (a) CFP pressure drop. The pressure drop through one unit with the porous medium simplified CFP and real CFP inlet and outlet zones is simulated. The temperature, mass flow rate and  $C_{VR}$  takes  $20\text{ }^\circ\text{C}$ ,  $0.01\text{ kg}\cdot\text{s}^{-1}\cdot\text{CFP}^{-1}$  and  $10^7\text{ m}^{-2}$  respectively. Six grid systems are examined. The simulated pressure drops between inlet and outlet are shown in Fig. 7. From Fig. 7, it can be seen that the results of the fourth grid system is 2.25% higher than that of the sixth grid system in the test condition. Therefore, the fourth grid system (grid number: 312 800) can be regarded as the grid-independent solution and is adopted in the following simulation.
- (b) Manifold pressure drop. The relationship between pressure drop and mass flow rate in a 75.2 mm stretch of manifold is simulated. The temperature takes  $20\text{ }^\circ\text{C}$ . Two grid systems are examined, in which the face grid numbers on the manifold cross section are 903 and 1 382 respectively. The simulated results are shown in Fig. 8. From Fig. 8, it can be seen that the maximum pressure drop relative deviation of the two grid systems is 1.8%. Therefore, the grid system with a manifold cross section grid number of 903 can be regarded as the grid-independent solution.
- (c) Coolant distribution curve of Case 0 in Table 1. In the following four tests, the CDCs of the PEMFC stacks introduced in Subsection 2.1.1 are simulated and the temperature takes  $69\text{ }^\circ\text{C}$ , which is the experimental average temperature of the coolant inlet and outlet surfaces in an on-line case. Four grid systems are examined, in which the face grid numbers on the manifold cross section are 2 091, 4 480, 8 385 and 16 560 respectively. Total grid numbers of the four grid systems are 57 780 808, 76 478 352, 106 889 238 and 170 943 600 respectively. The simulated results are shown in Fig. 9. From Fig. 9, it can be seen that the simulated result using the first grid system (2 091) will lead to wrong regular patterns at the begin and end of the CDC. Therefore, the second grid system (4 480) can be regarded as the grid-independent solution.
- (d) Coolant distribution curve of Case 2. Two grid systems are examined, in which the face grid numbers on the manifold cross section are 4 480 and 8 385 respectively. The simulated results are shown in Fig. 10. R-squared is 0.996, showing a high matching degree using the two grid systems. It can be seen that the first grid system (4 480) can be regarded as the grid-independent solution.

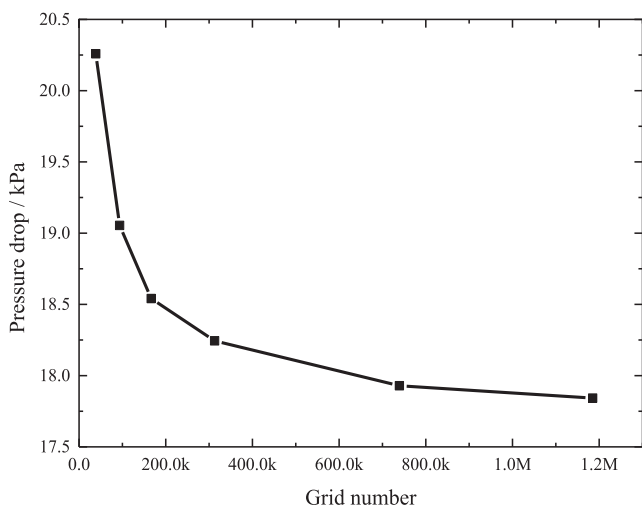


Fig. 7. Grid-independent test for coolant flow field pressure drop.

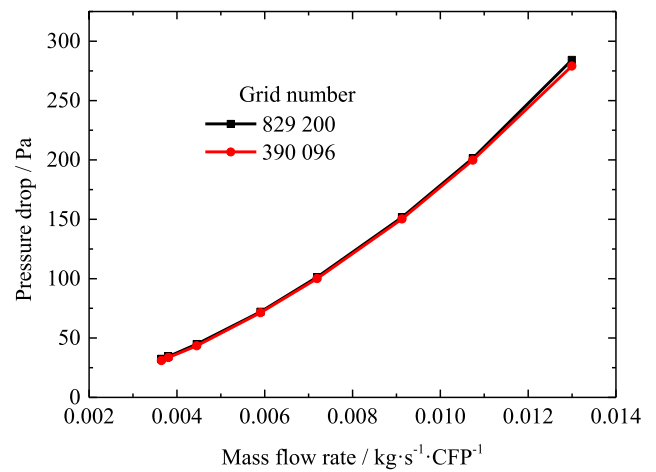


Fig. 8. Grid-independent test for manifold pressure drop.

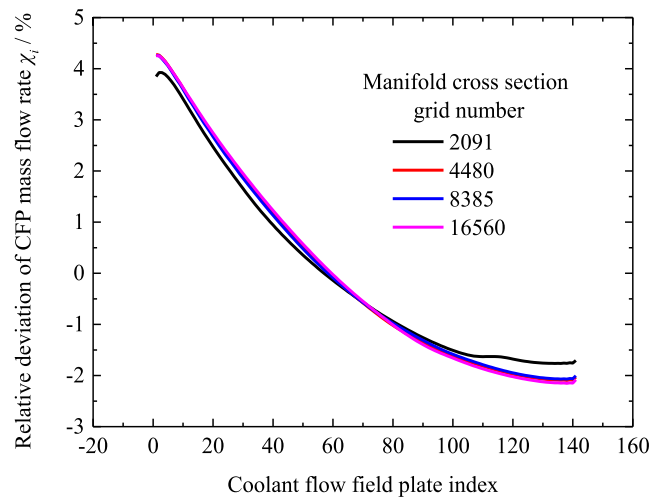


Fig. 9. Grid-independent test for coolant distribution curve of Case 0.

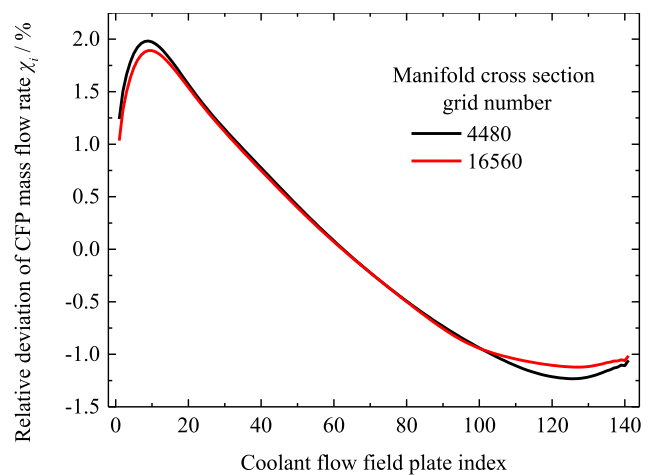


Fig. 10. Grid-independent test for coolant distribution curve of Case 2.

- (e) Coolant distribution curve of Case 3. Three grid systems are examined, in which the face grid numbers on the manifold cross section are 4 480, 8 385 and 16 560 respectively. The simulated results are shown in Fig. 11. It can be seen that the simulated results using the first grid system (4 480) will underestimate the

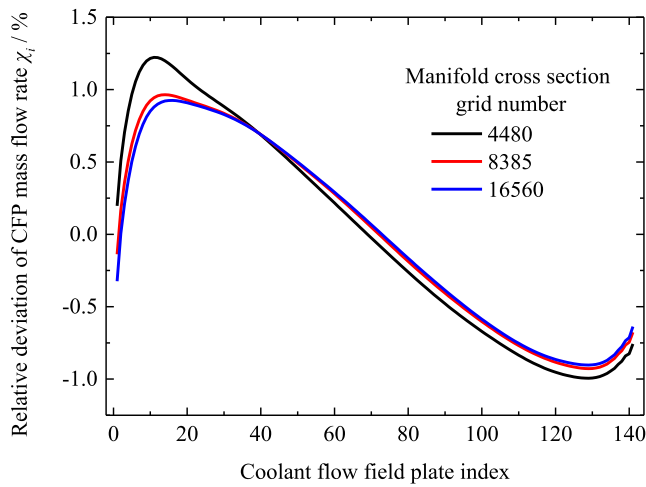


Fig. 11. Grid-independent test for coolant distribution curve of Case 3.

impact of the eccentric end socket on the begin of the CDC. Furthermore, R-squared between the CDCs using the second and third grid systems is 0.997. Therefore, the second grid system (8385) can be regarded as the grid-independent solution.

- (f) Coolant distribution curve of Case 4. Three grid systems are examined, in which the face grid numbers on the manifold cross section are 4480, 8385 and 33065 (total grid number: 298095750) respectively. The simulated results are shown in Fig. 12. R-squared between the CDCs using the second and third grid systems is 0.985. Therefore, the second grid system (8385) can be regarded as the grid-independent solution.

In summary, grid number tests of six aspects on the manifold cross section have been implemented. From the above six aspects of grid-independent tests, the grid independences for manifold pressure drop, CDC ( $0 \leq E_t \leq 0.7$ ) and CDC ( $0.7 < E_t \leq 1.0$ ) are summarized in Table 3. From Table 3, it can be seen that under the studied conditions, the grid independence for the pressure drop characteristics cannot guarantee the grid independence for the CDC, showing the necessity to test the CDC grid independence. Furthermore, due to a more complex flow field near the end socket, the grid independences under low and middle eccentricities cannot guarantee the grid independence under a high eccentricity, showing the necessity to test the grid independence under the most extreme working condition. Therefore, hereafter this paper, grid systems 4 and 5 are adopted if  $E$  ranges  $0 \leq E \leq 0.7$  and  $0.7 < E \leq 1.0$  respectively. Furthermore, in the analyses related to Cases 2, 3 and 4 in

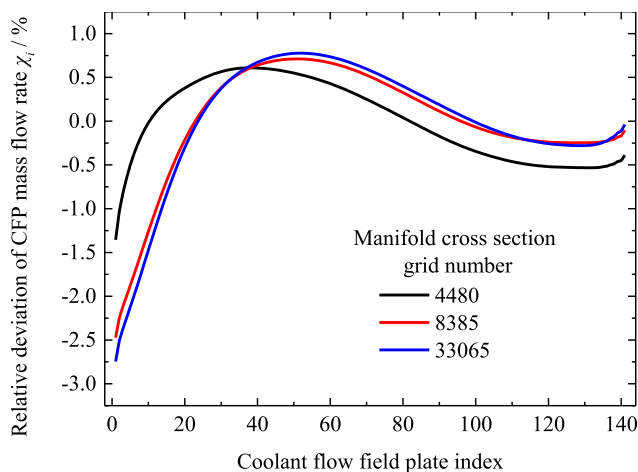


Fig. 12. Grid-independent test for coolant distribution curve of Case 4.

Table 3  
Summary of the grid-independent tests.

Grid system index	1	2	3	4	5	6	7
Manifold cross section grid number	903	1382	2091	4480	8385	16560	33065
Stack total grid number $\times 10^{-6}$	-	-	58	76	107	171	298
Manifold pressure drop	✓	✓	✓	✓	✓	✓	✓
CDC ( $0 \leq E \leq 0.7$ )	×	×	×	✓	✓	✓	✓
CDC ( $0.7 < E \leq 1.0$ )	×	×	×	×	✓	✓	✓

Table 1, the simulated results using the grid systems with the largest cell numbers in the grid-independent test process are adopted.

### 3.2.2. CDC comparison adopting different turbulent models

In the literatures, the standard and realizable  $k-\epsilon$  models are widely adopted. Case 2 in Table 1 is selected as an example to analyze the influence of turbulent model. The simulated results are shown in Fig. 13. R-squared between the two CDCs is 0.998, showing a high matching degree between the two turbulent models in the studied cases.

### 3.2.3. Experimental validation for the stack pressure drop

The stack pressure drop of the coolant plays an important role in a flow distribution and is important available information in the commercial-size PEMFC stack testing system. Therefore, the stack pressure drop is selected as a judgement for the validation of the established CFD model. The CFP number, eccentricity vector and temperature take 141, (0.42, 0.05) and  $20^\circ\text{C}$  respectively. The experimental results between pressure drop and mass flow rate, and the pressure drop in three simulated cases are shown in Fig. 14. It can be seen that the simulated pressure drops show a high consistence with the experimental ones, especially under the mass flow rate of  $0.01 \text{ kg}\cdot\text{s}^{-1}\cdot\text{CFP}^{-1}$  (corresponding current density:  $1.8 \text{ A}\cdot\text{cm}^{-2}$ ) which is the condition to be optimized hereafter, validating the reliability of the simulation model. Furthermore, it is sufficient to validate the cases with  $0.01 \text{ kg}\cdot\text{s}^{-1}\cdot\text{CFP}^{-1}$  in this paper. This is because that the maximum validated coolant mass flow rate condition corresponds to the highest working current density ( $1.8 \text{ A}\cdot\text{cm}^{-2}$ ) for the studied PEMFC stack. And it is for this current density case we work for the improvement of coolant flow distribution uniformity. Due to a heavy computing resource consumption for simulation, we think it is sufficient and economical to validate the case within  $0.01 \text{ kg}\cdot\text{s}^{-1}\cdot\text{CFP}^{-1}$  in this paper.

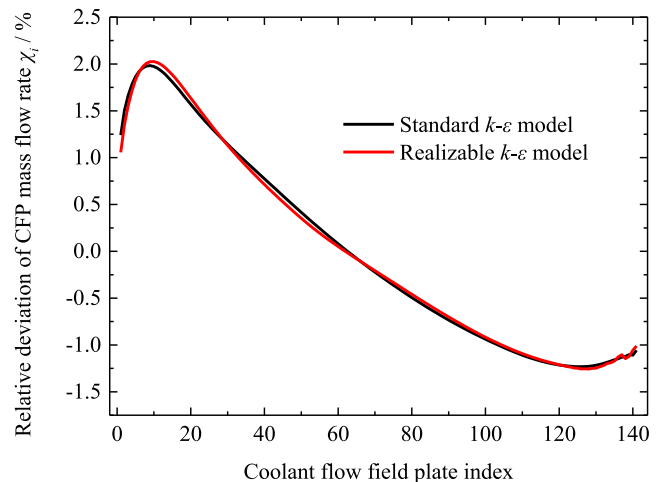


Fig. 13. Coolant distribution curve comparison adopting different turbulent models.

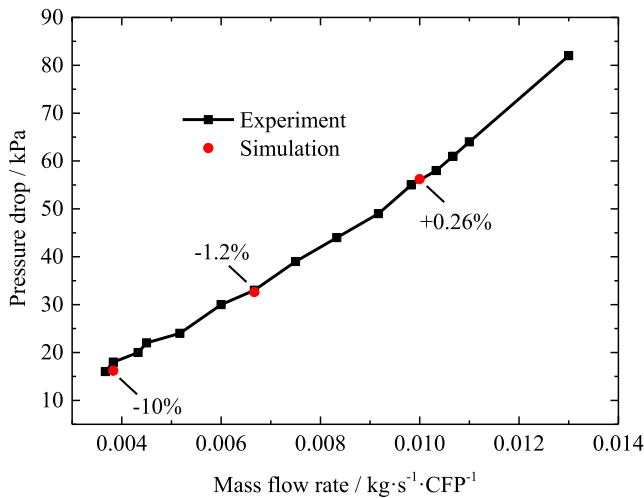


Fig. 14. Experimental validation for the stack pressure drop.

### 3.3. Impact of the eccentricity

Fig. 15 shows the impact of the eccentricity  $E$  on CDC when the argument  $\theta$  takes  $0^\circ$ . It can be seen that in general, with the CFP away from the stack inlet, the distributed coolant flow rate increases firstly, tends to decrease near the end, and finally increases slightly. The reason will be discussed in the following of this paragraph. Fig. 16 shows the streamline and pressure contour diagrams on the middle cross-section in the  $e_1$  direction in the inlet manifold under different  $E$ s. Fig. 17 shows the relative pressures on the inlet and outlet surfaces of each CFP as functions of the eccentricity. From Fig. 16, it can be seen that the vortex forms near the inlet end socket driven by the shear flow. Imaging an isolate region filled with static fluid, when a vortex is formed, the pressure at the center of the vortex is lower than that near the edge of the vortex. According to the vortex location in Fig. 16, the vortex (or flow rotating phenomenon) will lead to a high pressure gradient along the axial direction of the inlet manifold and a high gradient for the curve of CFP inlet pressure versus the CFP index, as shown in Fig. 17. As for the outlet manifold, although the eccentric structure is also adopted as the outlet end socket, it is located downstream of the outlet manifold, therefore shows small impact on the CFP outlet pressure distribution, as shown in Fig. 17. Therefore, with the increase of the CFP index, the pressure drop across a CFP will increase for the previous several CFPs. It is the pressure difference between a CFP inlet and outlet surfaces determine the mass flow rate through the CFP. Due to the identical

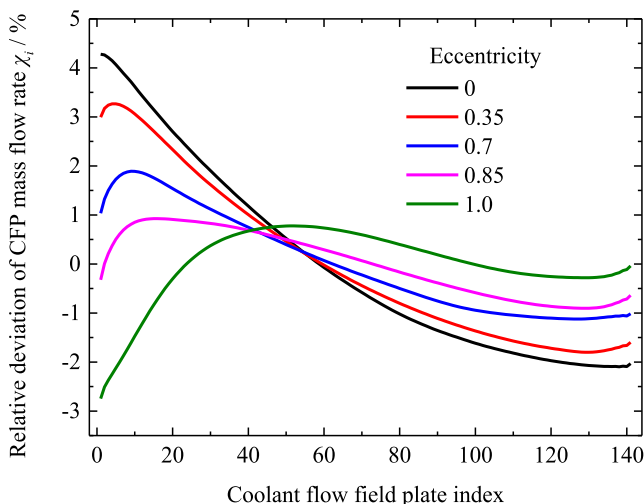


Fig. 15. Impact of the eccentricity magnitude on coolant distribution curve.

geometric structure for all the CFPs, their resistances are also identical. Therefore, for the previous several CFPs, the distributed coolant flow rate also increases with the increase of the CFP index. Furthermore, vortices or rotating flow also form near the end of the inlet manifold, as shown in Fig. 16. Similar with the above analyses, this is also the reason why the distributed coolant flow rate increases slightly at the end of the inlet manifold.

From Fig. 15, it can also be seen that with the increase of  $E$ , the mass flow rates of the first several CFPs decrease. Based on the analyses of the previous paragraph, this is because that with the increase of  $E$ , the vortex is more violent (as shown in Fig. 16), and thus the gradient of the CFP inlet pressure curve increases especially for the first several CFPs (as shown in Fig. 17). Furthermore, with the increase of  $E$ , the coolant distribution non-uniformity decreases firstly due to lower mass flow rates near the stack inlet. With the further increase of  $E$ , when  $\chi_1$  is lower than the lowest  $\chi_i$  near the end of the inlet manifold, the coolant distribution non-uniformity will finally increase. Therefore, a minimum coolant distribution non-uniformity exists. This is also the reason why the coolant distribution uniformity can be optimized by designing the eccentricity vector.

### 3.4. Impact of the argument

Fig. 18 shows the impact of the argument  $\theta$  on CDC when the eccentricity  $E$  takes 0.35. It can be seen that the CDCs are nearly identical if the eccentricity vector is axisymmetric with  $e_1$  ( $\theta = 90^\circ$ ) as axis. For example,  $0^\circ$  and  $180^\circ$ ,  $45^\circ$  and  $135^\circ$ ,  $-45^\circ$  and  $-135^\circ$ . This is because that the geometrical structure of the PEMFC stack is approximately axisymmetric.

From Fig. 18, it can also be seen that the CDCs are similar if the eccentricity vector  $E$  points to the same side of the  $e_1$  axis ( $\theta = 0^\circ$ ). For example:  $45^\circ$ ,  $90^\circ$  and  $135^\circ$ ;  $-45^\circ$ ,  $-90^\circ$  and  $-135^\circ$ . Contrarily, the CDCs are dissimilar if  $E$  points to the different sides of the  $e_1$  axis. Firstly, the gradient at the beginning of the CDC under  $-135^\circ \leq \theta \leq -45^\circ$  is lower than that under  $45^\circ \leq \theta \leq 135^\circ$ . This is due to different velocity vector distribution regular patterns, as shown in Fig. 19. It can be seen that driven by the end socket structure, the velocity component toward the CFP region under  $\theta = -90^\circ$  ( $-135^\circ \leq \theta \leq -45^\circ$ ) is larger than that under  $\theta = 90^\circ$  ( $45^\circ \leq \theta \leq 135^\circ$ ) at the beginning of the inlet manifold, leading to a better flow distribution. Therefore, the CDC gradient of the first thirty CFPs under  $-135^\circ \leq \theta \leq -45^\circ$  is lower. Furthermore, the gradient at the middle of the CDC under  $-135^\circ \leq \theta \leq -45^\circ$  is higher than that under  $45^\circ \leq \theta \leq 135^\circ$ . This is because that when  $\theta = 90^\circ$  ( $45^\circ \leq \theta \leq 135^\circ$ ), the flow rotating phenomenon (curvature of the streamline) in this region is more violent, as shown in Fig. 19. As is analyzed in Subsection 3.3, the more violent the flow rotating phenomenon is, the lower the CDC gradient is. Therefore, the CDC gradient at the middle of the CDC under  $45^\circ \leq \theta \leq 135^\circ$  is lower. Moreover, when  $\theta = -135^\circ$ ,  $-90^\circ$ ,  $-45^\circ$  and  $90^\circ$ , the slightly increasing trend at the end of CDC does not appear. This is because that in these cases, driven by the fluid viscosity, the vortex at the end of the inlet manifold is far from the CFP inlet region, as shown in the bottom right corner in Fig. 19 (a) and (b), showing an extremely low impact on CDC.

### 3.5. Design of the optimal eccentricity vector

According to the discussions in Subsections 3.3 and 3.4, the impact of  $E$  on CDC is much more prominent than  $\theta$ . Therefore,  $E$  is selected as the only design parameter for the eccentricity vector design and  $\theta$  takes 0.

Based on the simulated results of Cases 0 ~ 4 in Fig. 15, the mode space is constructed according to Subsection 2.2.1, as shown in Fig. 20. Case 1 is selected as an example to exhibit the predicted CDCs under different truncation orders, as shown in Fig. 21. From Fig. 20, it can be seen that mode 1 captures the most important CDC characteristics, for example, the lower distributed coolant flow rate near the stack inlet, the gradually decreasing impact of the vortex on distributed coolant flow

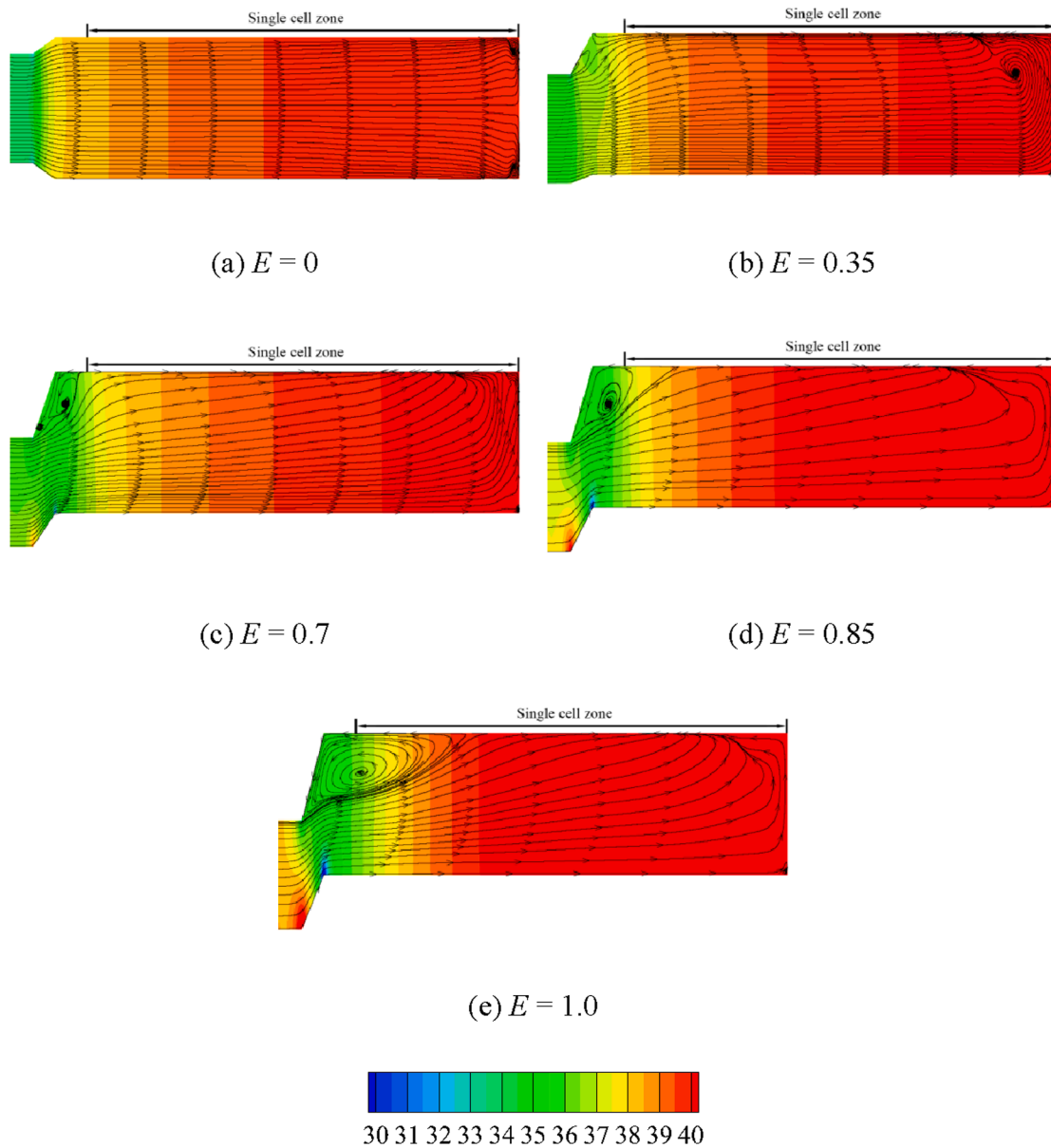


Fig. 16. Velocity vector and pressure (kPa) contour diagrams on the middle cross-section in the  $e_1$  direction in the inlet manifold under different eccentricity magnitude.

rate with the increase of the CFP index, and the slightly higher distributed coolant flow rate near the end of the inlet manifold. Therefore, the predicted CDC is close to the simulated one when the truncation order takes 1, as shown in Fig. 21. Furthermore, modes 2 and 3 slightly correct the local characteristics of CDC.

According to Subsection 2.2.2, the explicit mathematical expression between CDC and eccentricity is presented in Eq. (21).

$$\chi_i = \begin{cases} 23.26\psi_{i,0} + (7.696E^3 + 6.332E^2 + 8.046E)\psi_{i,1} \\ \quad + (19.82E^3 - 21.91E^2 + 3.378E)\psi_{i,2} \\ \quad + (-21.25E^3 + 25.82E^2 - 7.257E)\psi_{i,2} & 0 \leq E \leq 0.7 \\ 23.26\psi_{i,0} + (229.6E^3 - 459.7E^2 + 334.3E - 76.12)\psi_{i,1} \\ \quad + (17.24E^3 - 16.50E^2 - 0.4128E + 0.8845)\psi_{i,2} \\ \quad + (80.79E^3 - 188.5E^2 + 142.7E - 35.00)\psi_{i,3} & 0.7 \leq E \leq 1.0 \end{cases} \quad (21)$$

Then according to the analysis in Subsection 3.3, the coolant distribution uniformity can be optimized by Eq. (22).

$$\chi_1 - \min(\chi_{110 \sim 141}) = 0 \quad (22)$$

After solving Eq. (22) by the bisection method, the minimum non-uniformity is obtained as 1.58%. The corresponding  $E$  takes 0.8856 and the CDC are shown in Fig. 22. The non-uniformity reduces 4.04 times compared with that in the benchmark case (Case 0, 6.38%).

Even though the above results can only be adopted for the studied PEMFC stack, the proposed methodology has its wide application range to design better distributed manifold and end socket structures for the coolant, anode and cathode in PEMFC stacks, and even other similar heat exchange equipment.

#### 4. Conclusion

In this research, the coolant distribution curve of a practical commercial-size PEMFC stack with 141 coolant flow field plates is modelled by a 3D porous medium computational fluid dynamic

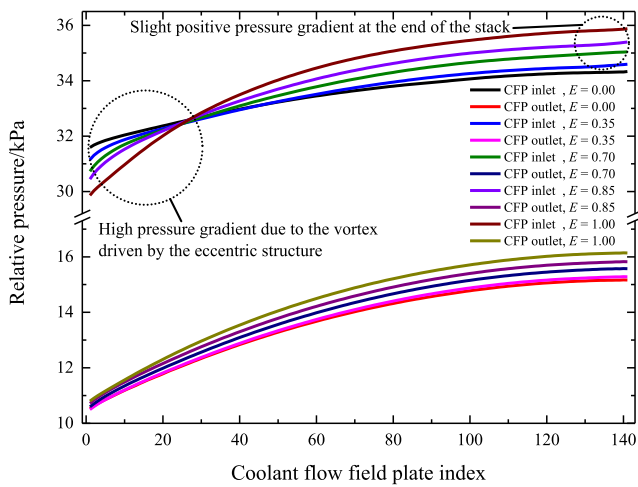


Fig. 17. Impact of the eccentricity magnitude on the relative pressure on the inlet and outlet surfaces of each coolant flow field plate (CFP).

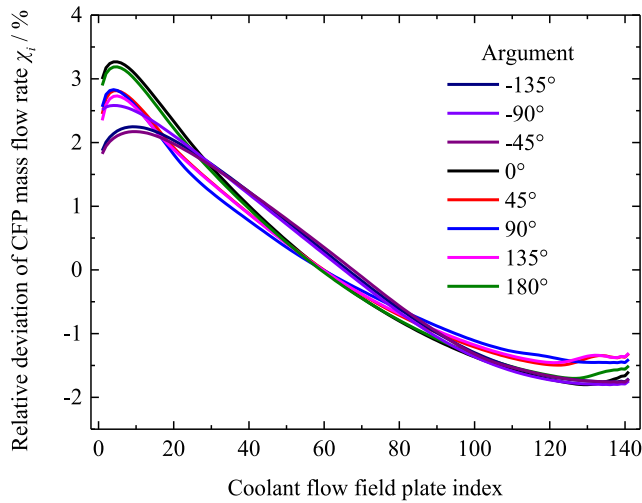


Fig. 18. Impact of the eccentricity argument on coolant distribution curve.

approach. The grid systems are comprehensively tested for the refined simulation requirements under a well-distributed condition and a high current density. A novel analysis model is proposed to further establish the explicit mathematical expression between coolant distribution curve and the eccentricity based on the CFD results and proper orthogonal decomposition method. The proposed methodology can reveal the explicit correlation according to a small amount of computational fluid dynamic cases (Cases 0 ~ 4), therefore, reduce the heavy burden of

computing resources in the manifold and end socket design. The coolant distribution uniformity is finally optimized based on the explicit expression.

The major conclusions of this paper are summarized as follows:

- (1) The grid independence for the pressure drop characteristics of the manifold and coolant flow field plate cannot guarantee the grid independence for the coolant distribution curve and the grid

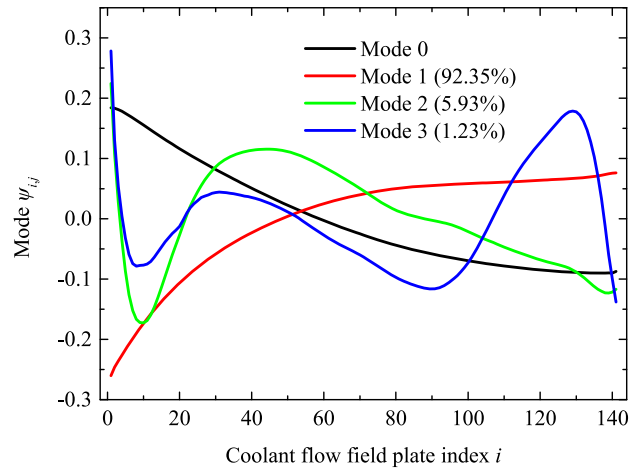


Fig. 20. Mode space for coolant distribution curve.

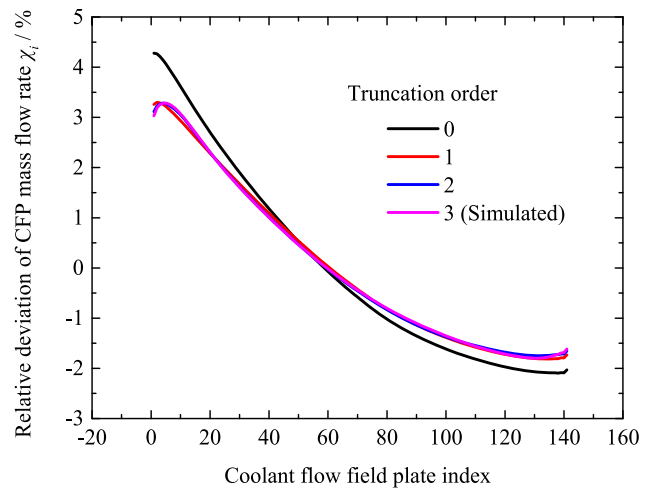


Fig. 21. Predicted coolant distribution curves under different truncation orders.

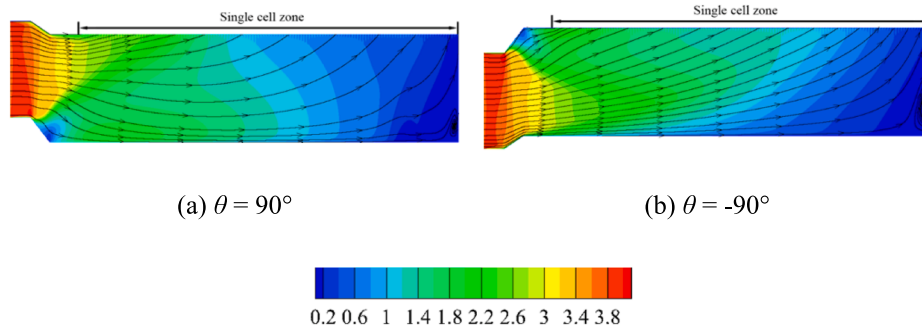


Fig. 19. Velocity vector and velocity magnitude ( $m \cdot s^{-1}$ ) contour diagrams on the middle cross-section in the  $e_t$  direction in the inlet manifold under different eccentricity arguments.

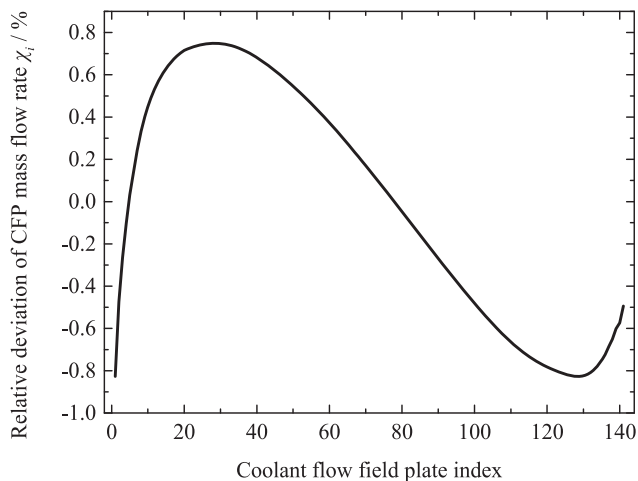


Fig. 22. Optimized coolant distribution curve.

independences under low and middle eccentricity cannot guarantee the grid independence under a high eccentricity. Within the range of this research, the grid systems with the manifold cross section grid numbers being 4 480 and 8 385 can be regarded as the grid-independent ones under the eccentricities ranging 0 ~ 0.7 and 0.7 ~ 1.0 respectively.

- (2) Driven by the eccentric end socket structure, with the coolant flow field plate away from the stack inlet, the coolant distribution curve increases firstly, tends to decrease near the end, and finally increases slightly when the eccentricity higher than 0.
- (3) The coolant distribution curves are nearly identical if the eccentricity vector is axisymmetric with the longitudinal eccentricity direction as axis. The coolant distribution curves are similar if the eccentricity vector points to the same side of the transverse eccentricity axis. When  $\theta$  takes  $-135^\circ$ ,  $-90^\circ$ ,  $-45^\circ$  or  $90^\circ$ , the slightly increasing trend at the end of coolant distribution curve does not appear.
- (4) With the increase of the eccentricity, the coolant distribution non-uniformity decreases firstly and finally increase. The optimized coolant distribution non-uniformity (1.58%) reduces 4.04 times compared with that in the benchmark case (6.38%). The corresponding optimal eccentricity takes 0.8856.

#### CRediT authorship contribution statement

**Fan Bai:** Conceptualization, Data curation, Formal analysis, Investigation, Methodology, Validation, Visualization, Writing – original draft, Writing – review & editing. **Ren-Jie Yin:** Investigation. **Jin-Yang Liao:** Funding acquisition, Supervision. **Zhuo Zhang:** Investigation. **Sai-Jie Cai:** Investigation. **Yu-Tong Mu:** Methodology. **Li Chen:** Project administration, Supervision. **Lei Chen:** Methodology. **Wen-Quan Tao:** Conceptualization, Funding acquisition, Project administration, Resources, Supervision, Writing – review & editing.

#### Declaration of Competing Interest

The authors declare that they have no known competing financial interests or personal relationships that could have appeared to influence the work reported in this paper.

#### Data availability

Data will be made available on request.

#### Acknowledgment

**Funding:** This work is supported by the National Key Research and Development Project of China [Grant number 2018YFB1502504], the key project of the National Natural Science Foundation of China [Grant number 51836005], the Foundation for Innovative Research Groups of the National Natural Science Foundation of China [Grant number 51721004], the Basic Research Project of Shaanxi Province [Grant number 2019ZDXM3-01] and the 111 Project [Grant number B16038]. The funding sources had no involvement in the investigation.

#### References

- [1] Li D, Park EJ, Zhu W, Shi Q, Zhou Y, Tian H, et al. Highly quaternized polystyrene ionomers for high performance anion exchange membrane water electrolyzers. *Nat Energy* 2020;5(5):378–85.
- [2] Bai F, Lei L, Zhang Z, Chen L, Chen L, Tao WQ. Application of similarity theory in the study of proton exchange membrane fuel cells: A comprehensive review of recent developments and future research requirements. *Energy Storage Saving* 2022;1(1):3–21.
- [3] Hu D, Wang Y, Li J, Yang Q, Wang J. Investigation of optimal operating temperature for the PEMFC and its tracking control for energy saving in vehicle applications. *Energ Convers Manage* 2021;249:114842.
- [4] Su G, Yang D, Xiao Q, Dai H, Zhang C. Effects of vortices in feed header on air flow distribution of PEMFC stack: CFD simulation and optimization for better uniformity. *Renew Energy* 2021;173:498–506.
- [5] Amirfazli A, Asghari S, Koosha M. Mathematical modeling and simulation of thermal management in polymer electrolyte membrane fuel cell stacks. *J Power Sources* 2014;268:533–45.
- [6] Kandlikar SG, Lu Z. Thermal management issues in a PEMFC stack—A brief review of current status. *Appl Therm Eng* 2009;29(7):1276–80.
- [7] Choi EJ, Park JY, Kim MS. A comparison of temperature distribution in PEMFC with single-phase water cooling and two-phase HFE-7100 cooling methods by numerical study. *Int J Hydrogen Energy* 2018;43(29):13406–19.
- [8] Wang C, Li Q, Wang C, Zhang Y, Zhuge W. Thermodynamic analysis of a hydrogen fuel cell waste heat recovery system based on a zeotropic organic Rankine cycle. *Energy* 2021;232:121038.
- [9] Zhang G, Kandlikar SG. A critical review of cooling techniques in proton exchange membrane fuel cell stacks. *Int J Hydrogen Energy* 2012;37(3):2412–29.
- [10] Konno N, Mizuno S, Nakaji H, Ishikawa Y. Development of compact and high-performance fuel cell stack. *SAE Int J Alternative Powertrains* 2015;4(1):123–9.
- [11] Wei L, Dafalla AM, Jiang F. Effects of reactants/coolant non-uniform inflow on the cold start performance of PEMFC stack. *Int J Hydrogen Energy* 2020;45(24):13469–82.
- [12] Huang F, Qiu D, Lan S, Yi P, Peng L. Performance evaluation of commercial-size proton exchange membrane fuel cell stacks considering air flow distribution in the manifold. *Energ Convers Manage* 2020;203:112256.
- [13] Huang F, Qiu D, Xu Z, Peng L, Lai X. Analysis and improvement of flow distribution in manifold for proton exchange membrane fuel cell stacks. *Energy* 2021;226:120427.
- [14] Koh JH, Seo HK, Lee CG, Yoo YS, Lim HC. Pressure and flow distribution in internal gas manifolds of a fuel-cell stack. *J Power Sources* 2003;115(1):54–65.
- [15] Chang PA, St-Pierre J, Stumper J, Wetton B. Flow distribution in proton exchange membrane fuel cell stacks. *J Power Sources* 2006;162(1):340–55.
- [16] Wang J. Pressure drop and flow distribution in parallel-channel configurations of fuel cells: U-type arrangement. *Int J Hydrogen Energy* 2008;33(21):6339–50.
- [17] Wang J. Pressure drop and flow distribution in parallel-channel configurations of fuel cells: Z-type arrangement. *Int J Hydrogen Energy* 2010;35(11):5498–509.
- [18] Qin Y, Liu G, Chang Y, Du Q. Modeling and design of PEM fuel cell stack based on a flow network method. *Appl Therm Eng* 2018;144:411–23.
- [19] Amirfazli A, Asghari S, Sarraf M. An investigation into the effect of manifold geometry on uniformity of temperature distribution in a PEMFC stack. *Energy* 2018;145:141–51.
- [20] Bai X, Luo L, Huang B, Huang Z, Jian Q. Flow characteristics analysis for multi-path hydrogen supply within proton exchange membrane fuel cell stack. *Appl Energy* 2021;301:117468.
- [21] Chen CH, Jung SP, Yen SC. Flow distribution in the manifold of PEM fuel cell stack. *J Power Sources* 2007;173(1):249–63.
- [22] Mustata R, Valino L, Barreras F, Gil MI, Lozano A. Study of the distribution of air flow in a proton exchange membrane fuel cell stack. *J Power Sources* 2009;192(1):185–9.
- [23] Shimpalee S, Ohashi M, Van Zee JW, Ziegler C, Stoeckmann C, Sadeler C, et al. Experimental and numerical studies of portable PEMFC stack. *Electrochim Acta* 2009;54(10):2899–911.
- [24] Huang F, Qiu D, Peng L, Lai X. Entrance Effects on the Flow Distribution in Manifold of Commercial-Size Proton Exchange Membrane Fuel Cell Stacks. *ECS Trans* 2019;92(8):375–85.
- [25] Li M, Duan K, Djilali N, Sui PC. Flow sharing and turbulence phenomena in proton exchange membrane fuel cell stack headers. *Int J Hydrogen Energy* 2019;44(57):30306–18.

- [26] Chen WH, Tsai ZL, Chang MH, You S, Kuo PC. Geometry optimization and pressure analysis of a proton exchange membrane fuel cell stack. *Int J Hydrogen Energy* 2021;46(31):16717–33.
- [27] Dai JQ, Yang ZM, Wang WS, Liu JP, Akenteng YD, Chen DF. Study the flow and species distribution characteristics in a typical 25-cell proton ceramic fuel cell stack by 3D large-scale modeling. *Ionics* 2022;28(4):1863–72.
- [28] Huang F, Qiu D, Peng L, Lai X. Optimization of entrance geometry and analysis of fluid distribution in manifold for high-power proton exchange membrane fuel cell stacks. *Int J Hydrogen Energy* 2022;47(52):22180–91.
- [29] Pan W, Chen Z, Chen X, Wang F, Dai G. Analytical and numerical investigation of flow distribution in PEMFC stacks. *Chem Eng J* 2022;450:137598.
- [30] Chmielewski M, Gieras M. Three-zonal wall function for  $k\text{-}\epsilon$  turbulence models. *Computat Methods Sci Technol* 2013;19(2):107–14.
- [31] Bai F, Lei L, Zhang Z, Li H, Yan J, Chen L, et al. Application of similarity theory in modeling the output characteristics of proton exchange membrane fuel cell. *Int J Hydrogen Energy* 2021;46(74):36940–53.
- [32] **Fluent help file**; 2020. <https://ansyshelp.ansys.com>.
- [33] Brinkman HC. A calculation of the viscous force exerted by a flowing fluid on a dense swarm of particles. *Flow Turbul Combust* 1949;1:27–34.
- [34] Breugem WP. The effective viscosity of a channel-type porous medium. *Phys Fluids* 2007;19(10):103104.
- [35] Cameron AC, Windmeijer FA. An R-squared measure of goodness of fit for some common nonlinear regression models. *J Econ* 1997;77(2):329–42.
- [36] Bai F, Quan HB, Yin RJ, Zhang Z, Jin SQ, He P, et al. Three-dimensional multi-field digital twin technology for proton exchange membrane fuel cells. *Appl Energy* 2022;324:119763.